ACS APPLIED MATERIALS & INTERFACES

www.acsami.org

Research Article

Porous Carbon Nanosheets Armoring 3D Current Collectors toward Ultrahigh Mass Loading for High-Energy-Density All-Solid-State Supercapacitors

Jing Zhan,[§] Gaoran Li,[§] Qihang Gu, Hao Wu, Liwei Su,* and Lianbang Wang*

Cite This: *ACS Appl. Mater. Interfaces* 2021, 13, 52519–52529

Read Online

ACCESS | Metrics & More | Article Recommendations | Supporting Information

ABSTRACT: The in situ growth of active materials on 3D current collectors (such as Ni foams) presents facile and efficient access to high-performance supercapacitors. However, the low surface area of current collectors limits the mass loading, microstructure, and capacitive performance of active materials thereon. Herein, we develop a novel surface modification with hierarchical N-rich carbon nanosheets on Ni foams via a simple sol−gel method. At the same time, its favorable effects on mass loading and utilization are demonstrated using NiCoMn-carbonate hydroxide (NCM) as a model active material. Specifically, the carbon modification greatly boosts the current collector's specific surface area and enables the growth of dense NCM nanoneedles with controllable mass loading ranging from 5.2 to 23.1 mg cm^{-2}. Meanwhile, the correlation between mass loading and utilization is systematically studied, which shows the well-maintained energy storage efficiency due to the conducive surface modification. As a result, excellent performance with the ultrahigh area-specific capacity of 19.36 F cm^{-2} at 2 mA cm^{-2} in the three-electrode configuration and remarkable area-specific energy density of 1352 μW h cm^{-2} in the solid-state asymmetric device can be achieved, demonstrating a prospective pathway toward facile and effective current collector designs for high-energy/power-density supercapacitors.

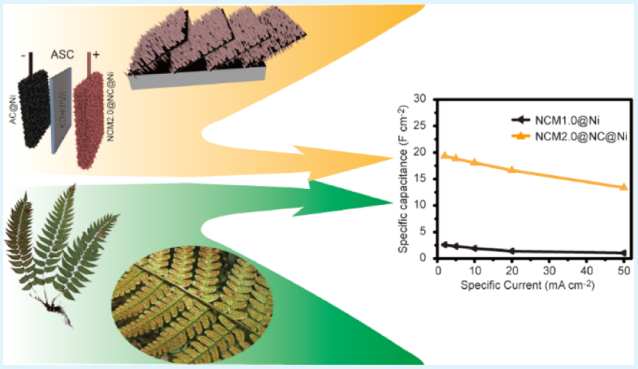

KEYWORDS: *surface modification, mass loading, nickel foams, area-specific energy density, solid-state supercapacitors*

1. INTRODUCTION

High-efficiency energy storage devices can compensate for the intermittency of renewable energy such as solar and wind, hence playing an essential role in dispatchable energy systems and portable electrics. Supercapacitors (SCs) are among the most promising candidates due to their long lifespan, high-power density, and excellent rate capability.[1−4] However, the mass- and area-specific energy densities of SCs are relatively lower than their battery counterparts, which severely hampers their practical and widespread applications.[5−7] Therefore, increasing the areal specific energy density is crucial yet challenging without sacrificing power density and longevity.

$$E = CU^2/2 \quad (1)$$

$$C_a = nmC_t \quad (2)$$

According to eqs 1 and 2, the area-specific energy density (E) depends on the voltage window (U) and area-specific capacitance (C_a), which closely relate to the mass utilization (n), mass loading (m), and the theoretical capacitance (C_t) of active materials.[3,8] The voltage window (U) can be widened using nonaqueous electrolytes or assembling them into asymmetric configurations. The mass utilization (n) can be promisingly boosted by nano-engineering and compositing techniques that enhance the specific surface area (SSA) and ion/electron conductivity. In addition, the mass loading (m) depends on advanced electrode designs, such as active materials' in situ growth on 3D current collectors, while the theoretical capacitance (C_t) is determined by the intrinsic physicochemical nature of the active materials employed.

Remarkably, the mass loadings of electrodes prepared by the conventional slurry-pasting method are generally less than 2.0 mg cm^{-2},[9−14] far lower than the industry requirement (∼10 mg cm^{-2}).[15−18] Moreover, polymer binders, conductive additives, and solvents inevitably reduce the overall capacitance and increase production costs. In this context, the in situ growth of active materials directly on the 3D conductive matrix, for example, Ni foams, due to high conductivity, strong

Received: July 10, 2021
Accepted: October 20, 2021
Published: October 30, 2021

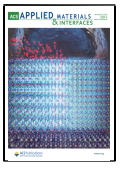

https://doi.org/10.1021/acsami.1c12953
ACS Appl. Mater. Interfaces 2021, 13, 52519−52529

alkali resistance, uniform pore structure, and good mechanical strength, are emerging as an alternative fabrication technology and attracting extensive attention.[19−23] The obtained self-standing electrodes can avoid using additional inactive materials and the complicated preparation procedures and enable the tight binding of active materials on the current collector with the concurrent prevention of material agglomeration. However, traditional Ni foams are facing some bottlenecks in this scenario, which can be exemplified by its intrinsically small SSA that severely limits the mass loading capability (generally 0.8−5.0 mg cm^{-2}).[24−28] To the best of our knowledge, the previously reported highest mass loading of the in situ grown active materials on the Ni foam was ∼18 mg cm^{-2},[29] showing an area-specific capacitance of 2.79 F cm^{-2}. Apart from that, Ni foams' surface characters (specific area, composition, and microstructure) also affect the structure, composition, and binding strength of active materials thereon. Therefore, it is essential to modify the surface of Ni foams with a higher SSA and more favorable chemical composition.

Ni foam modification is receiving more attention in both academia and industry. The strategies can be divided into (i) preparation process modification and (ii) surface modification. (i) Ni foams are generally prepared using polyurethane as a hard template and successively treated through chemical pretreatment, Ni electrodeposition, and heating. Optimizing the template and processing technology can adjust Ni foams' composition, structure, and properties.[30−33] (ii) Surface modification refers to the surface corrosion,[34] carbon coating,[35−38] electrodeposition,[39] oxidation,[40,41] replacement,[42] and so forth. The carbon coating can increase the SSA, elevate electronic conductivity, and provide extra functions. However, it is still challenging to achieve high-mass-loading capacitors by optimizing the surface nature of Ni foam. To the best of our knowledge, both the N-rich carbon nanosheet-modified Ni foam and its application in SCs are not reported until now.

Based on these considerations, herein, a rational surface modification on Ni foam current collectors by hierarchical N-rich carbon nanosheets (denoted as NC@Ni) was developed to improve the mass loading (m) and mass utilization (n) of active materials simultaneously. Carbonate hydroxides are employed to show the influence of the carbon nanosheet modification due to their merits for intercalation spacing and diverse morphology.[43,44] Considering that multicomponent materials synergistically affect the whole performance, we adopted ternary NiCoMn-carbonate hydroxide (NCM for short) as a case study rather than single metal compounds. It was revealed that the carbon modification boosted the SSA of Ni foam, thereby enabling the uniform growth of NCM nanoneedles with controllable and high mass loadings (5.2−23.1 mg cm^{-2}). Compared with a fresh Ni foam, the NC@Ni offered higher mass loadings and significantly superior electrochemical performances, particularly in the area-specific capacitance. Beyond that, an expanded voltage window (U) of 1.6 V and an outstanding area-specific energy density of 1352 μW h cm^{-2} were realized in solid-state asymmetric capacitors (ASC) configuration, demonstrating the great promise of the as-developed NC@Ni current collector design in the development of high-performance SCs.

2. EXPERIMENTAL SECTION

2.1. Carbon Modification of Nickel Foams. All the chemicals were of analytical grade and used without purification. Before the carbon modification, Ni foams (>99.8% Ni; 1.5 mm thick; 380 g m^{-2} surface density; 95% porosity; Taiyuan yingze, China) were cleaned using a 3 M HCl solution (10 min) and deionized (DI) water under sonication to remove the surface impurities. The carbon nanosheet modification on Ni foams was conducted via a simple sol−gel method. Typically, Ni foams (1.0 cm × 4.0 cm) were placed in a mixed solution of 0.8 g of $Ni(CH_3COO)_2{\cdot}6H_2O$ (Aladdin), 1.0 g of citric acid (Aladdin), 10 g of urea (99%, Aladdin), 75 mL of DI water, and 25 mL of CH_3CH_2OH (99.7%, Anhui Ante Food Co., Ltd), transferred into a water bath and maintained at 80 °C until all the DI water and ethanol are volatile. The product was dried in a vacuum oven at 60 °C for 12 h. Finally, the product was heated at 350 and 650 °C for each 2 h in Ar to obtain the NC@Ni. The Ni foams changed from silver to black after the carbon coating.

2.2. Synthesis of NCM Nanoneedles. Metal carbonate hydroxides can present higher rate capability and superior cycle stability than oxides and hydroxides.[45,46] Ternary NCM could balance the cost, safety, and electrochemical performance well, likely due to the synergistic effect among metals.[11] Thus, NCM was employed as a model active material to demonstrate the impact of carbon modification in this work. The NCM nanoneedles were planted on a NC@Ni and fresh Ni foam via a one-pot hydrothermal route. First, 2 mmol $NiCl_2{\cdot}6H_2O$, 2 mmol $CoCl_2{\cdot}6H_2O$, 2 mmol $MnCl_2{\cdot}4H_2O$, and 1.352 g of urea were dispersed to 30 mL of H_2O under stirring to obtain a homogeneous solution. Together with a piece of NC@Ni (or Ni), the obtained pink solution was transferred into a Teflon-lined autoclave (50 mL), sealed, and kept at 120 °C for 6 h. After cooling down to room temperature, the product was washed with DI water and ethanol and then dried in vacuum at 60 °C to obtain the final product. Similarly, a series of metallic salts and urea amounts were used to tune the mass loading of NCM on both substrates. The final products were denoted as NCMX@NC@Ni or NCMX@Ni, where X refers to the amount (mmol) of single metallic salt (Table S1).

2.3. Materials Characterization. The crystalline phases of all the samples were analyzed using X-ray diffraction (XRD, PANalytical X'Pert Pro X-ray, Cu Kα radiation, λ = 1.5418 Å, scan rate: 2° min^{-1}). The surface component was studied in a Thermo Scientific K-Alpha+ X-ray photoelectron spectroscopy (XPS) system. Fourier transform infrared (FTIR) were carried out in a Nicolet iS5 FTIR in 400−4000 cm^{-1}. Raman spectra were performed in a Raman spectrometer (LabRam HR Evolution). The SSA was characterized using N_2 adsorption−desorption apparatus (ASAP2460). The morphology, microstructure, and element distribution were confirmed using scanning electron microscopy (SEM, Zeiss Gemini500), high-resolution transmission electron microscopy (HRTEM, Tecnai G2F30, FEI), selected area electron diffraction (SAED, Tecnai G2F30, FEI), energy-dispersive X-ray (EDX) mapping, and linear scanning mapping (Tecnai G2F30, FEI).

2.4. Electrochemical Measurement. The electrochemical performance was characterized using NCMX@NC@Ni or NCMX@Ni as the working electrode (1.0 cm × 1.0 cm), Hg/HgO as the reference electrode, Pt foil as the counter electrode, and 3 M KOH solution as the electrolyte. Apart from that, the solid-state ASC performance was evaluated in a two-electrode configuration using the NCM2.0@NC@Ni as the cathode, activated carbon (AC) as the anode, and polyvinyl acetate (PVA)/KOH solid films as the electrolyte and separator. To prepare the PVA/KOH electrolyte, 5 g of PVA (M_w: 89,000−98,000, 99% hydrolyzed, Aldrich) was dissolved in 30 mL of DI water at 85 °C until the solution became apparent, and 8.4 g of KOH was dissolved in a beaker with 20 mL of DI water. The two solutions were mixed under stirring for 2 h to obtain a gel mixture at room temperature. For ASC assembly, the PVA/KOH electrolyte was coated on the electrode surface. After evaporating water at room temperature, the two electrodes were recoated with the PVA/KOH electrolyte and pressed together. The AC electrode was obtained by casting the slurry consisting of 80 wt % AC, 10 wt % acetylene black, and 10 wt % poly(vinylidene fluoride) on Ni foams and dried at 60 °C for 12 h.

Cyclic voltammetry (CV) curves, galvanostatic charge−discharge (GCD) profiles, and electrochemical impedance spectroscopy (EIS) plots were collected on a CHI660B electrochemical workstation

https://doi.org/10.1021/acsami.1c12953
ACS Appl. Mater. Interfaces 2021, 13, 52519−52529

Scheme 1. Schematic for the Modification Process of Ni Foams and the Preparation of NCM@NC@Ni and NCM@Ni Composites

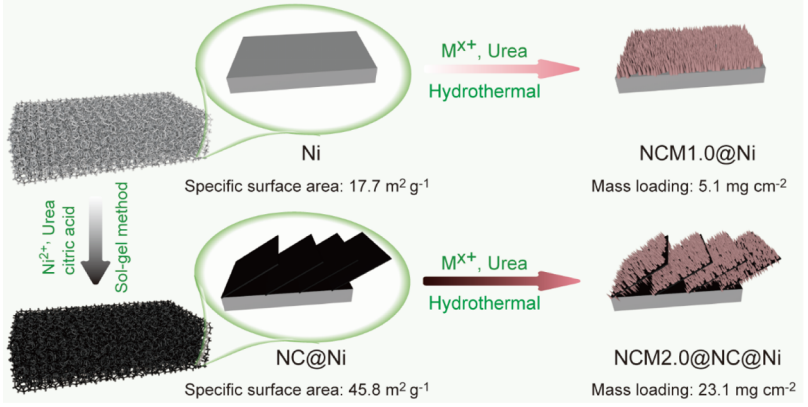

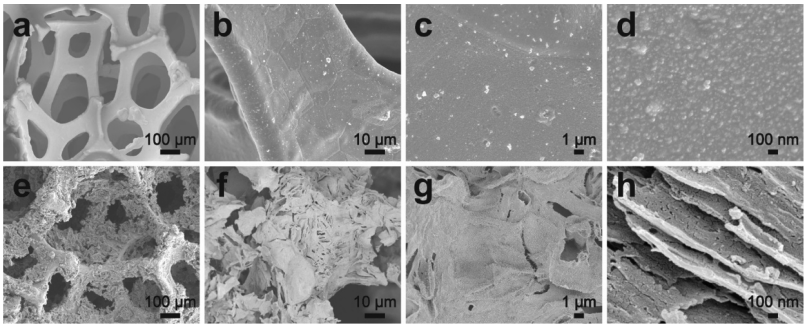

Figure 1. SEM images of (a–d) fresh Ni foams and (e–h) NC@Ni current collectors.

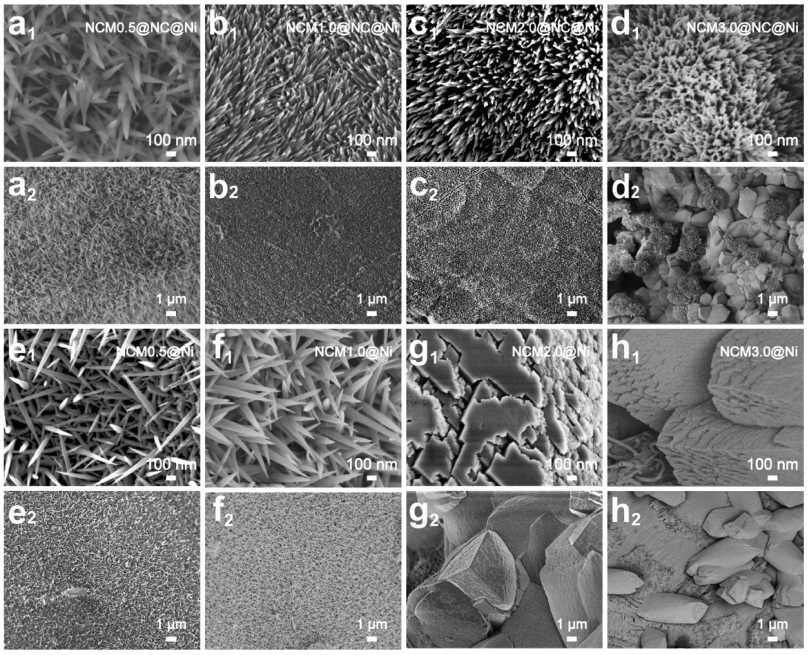

Figure 2. SEM images of NCM*X*@NC@Ni: (a_1,a_2) X = 0.5, (b_1,b_2) X = 1.0, (c_1,c_2) X = 2.0, and (d_1,d_2) X = 3.0 and NCM*X*@Ni: (e_1,e_2) X = 0.5, (f_1,f_2) X = 1.0, (g_1,g_2) X = 2.0, and (h_1,h_2) X = 3.0.

(Chenhua, Shanghai) at room temperature. EIS was carried out at 10 mHz to 100 kHz with an amplitude of 5 mV.

3. RESULTS AND DISCUSSION

3.1. Material Structure and Composition Characterization. Scheme 1 shows the preparation of NC@Ni, NCM@NC@Ni, and NCM@Ni. The carbon nanosheet modification was conducted by dipping a Ni foam into the precursor gel solution, then removing the excess solvent and thermal treatment, which turned the silver Ni foam into black NC@Ni with a considerable enrichment of the surface nanostructure. After that, the NCM nanoneedles were planted on the

https://doi.org/10.1021/acsami.1c12953
ACS Appl. Mater. Interfaces 2021, 13, 52519–52529

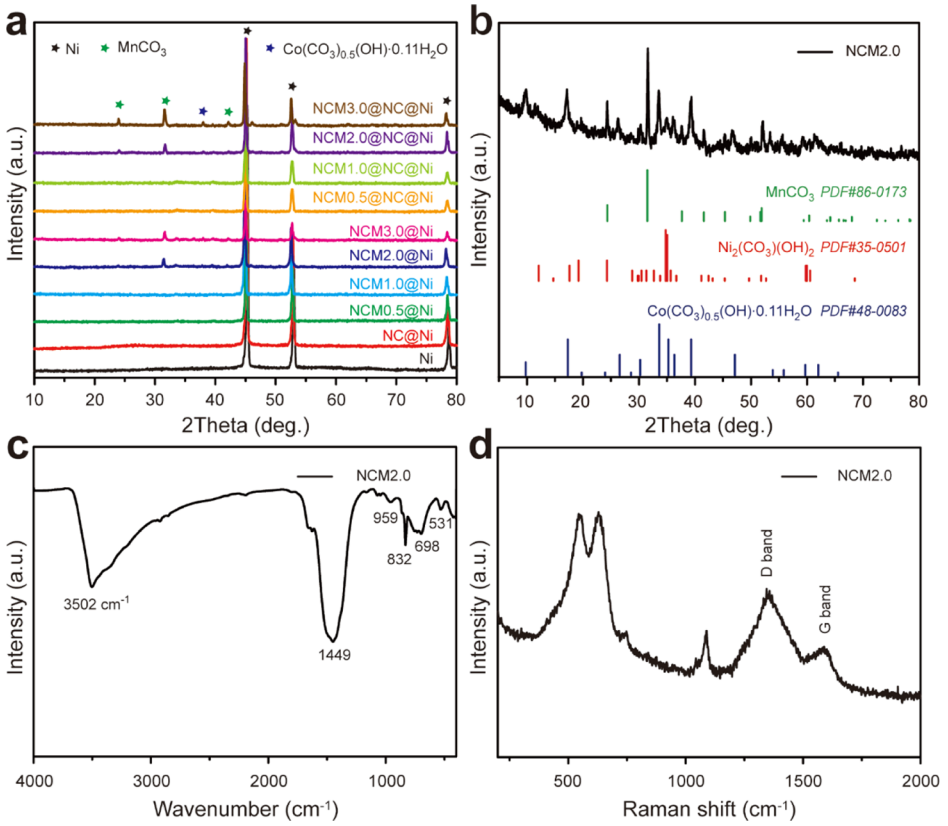

Figure 3. (a) XRD patterns of all the NCM samples. (b) XRD patterns, (c) FTIR, and (d) Raman spectrum of the NCM2.0 powder deprived of the NC@Ni substrate.

NC@Ni substrate using a hydrothermal method to yield NCM@NC@Ni composites. The reaction mechanism can be generally understood as follows[45,47]

$$CO(NH_2)_2 + H_2O \rightarrow CO_2 + 2NH_3 \quad (3)$$

$$CO_2 + H_2O \rightarrow CO_3^{2-} + 2H^+ \quad (4)$$

$$NH_3 + H_2O \rightarrow NH_4^+ + OH^- \quad (5)$$

$$2M^{2+} + CO_3^{2-} + 2OH^- \rightarrow M_2(CO_3)(OH)_2 \quad (M = Co, Ni, Mn) \quad (6)$$

The mass loading of NCM on NC@Ni can be controlled by the dosage of metal salt upon the hydrothermal process, offering a high mass loading of 23.1 mg cm^{-2} for NCM2.0. By contrast, the absence of carbon modification results in significantly less NCM loading on fresh Ni foams. More detailed studies were performed below.

The surface morphologies of the fresh Ni foam and NC@Ni were studied using SEM observations. Figure 1a shows that the pristine Ni foam consists of robust Ni skeletons with a relatively smooth surface, while the magnified SEM images (Figure 1b–d) witness the massive Ni nanodots thereon. By sharp contrast, the skeleton of NC@Ni is covered by abundant carbon nanosheets, exhibiting a rough surface as shown in Figure 1e,f. The carbon nanosheets deliver a substantial planar width over 20 μm (Figure 1g) and a layered structure consisting of nanosheets in thickness of ~20 nm (Figure 1h). Moreover, the carbon nanosheets interconnect to form slit-like channels for interface exposure and ion transfer. According to the mass change before and after the modification, the carbon content is ~10 wt % in the obtained NC@Ni. In addition, carbon nanosheets derived from the precursor without Ni support were also prepared. As shown in Figure S1, they consistently exhibit the multilayered structure with large lamellar spacing. The enriched N heteroatomic doping (~30 wt %) and massive Ni nanoparticles (~32 wt %) in the carbon nanosheets have been demonstrated in our previous work.[48]

Figure S2 shows the N_2 adsorption–desorption isotherm of the fresh Ni foam, carbon nanosheets, and NC@Ni. The isotherm curve of the pristine Ni foam overlap at the broad P/P_0 range of 0–0.95, suggesting the relatively weak N_2–Ni interaction (Figure S2a).[49] The SSA of Ni foam is only 17.7 m^2 g^{-1}. By comparison, the carbon nanosheets show an IV-type isotherm with an H3 type hysteresis loop (Figure S2b), indicating the abundance of mesopores.[50] The SSA of pure carbon nanosheets is 301.2 m^2 g^{-1}. The isotherm of the NC@Ni is shown in Figure S2c. The curve rises steadily and increases P/P_0 without distinct inflection, implying an entirely different surface character. The SSA of NC@Ni is 45.8 m^2 g^{-1}. The significantly boosted SSA from Ni to NC@C provides more sites for the growth of active materials and thus enables higher loading capability.

SEM images (Figure 2) were collected to determine the morphological evolution of the NCM on both substrates. Figure 2a–d shows that NCM nanoneedles vertically anchor on the NC@Ni surface. These regular nanoneedles become denser as the metal amount increases from 0.5 to 2.0 mmol in the precursor solution. The high-density nanoneedles offer a highly exposed surface and high mass loading for electrochemical reactions. The NCM mass loading at 0.5, 1.0, and 2.0 mmol metal dosage is 5.2, 10.6, and 23.1 mg cm^{-2},

https://doi.org/10.1021/acsami.1c12953
ACS Appl. Mater. Interfaces 2021, 13, 52519–52529

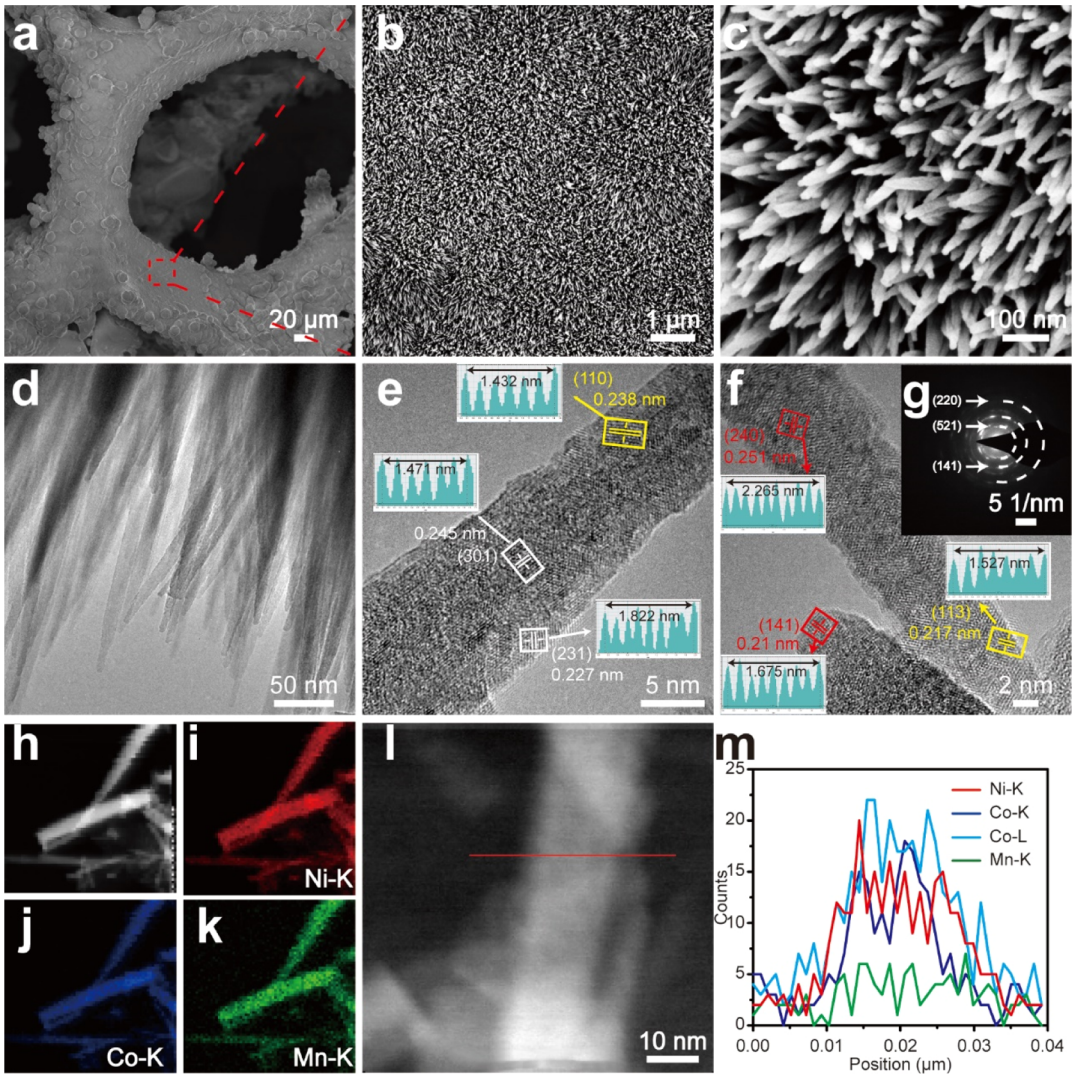

Figure 4. Microstructure characterization of the NCM2.0: (a–c) SEM images with different magnifications, (d) TEM image, (e,f) HRTEM images, (g) SAED pattern, and (h–k) EDX mapping images: (h) survey, (i) Ni–K, (j) Co–K, and (k) Mn–K, (l,m) linear scanning of element distribution in the nanoneedle.

respectively. However, the nanoneedles partially agglomerate into microspheres and even transform into bulky structures when the metal was raised to 3.0 mmol with a resulting mass loading of 40.8 mg cm^{-2} (Figures 2d and S3). This result suggests a loading limit for NC@Ni to maintain the nanoneedle structure of NCM thereon. By sharp contrast, the pristine Ni foam exhibits a much lower loading capacity, resulting in NCM mass loading of 3.2 and 5.1 mg cm^{-2} at low metal amounts of 0.5 and 1.0 mmol, respectively (Figure 2e,f). Serious agglomeration and morphological deformation can be observed at higher loadings, which is detrimental to the exposure of active interfaces for capacitive storage (Figure 2g,h). Therefore, it is confirmed that the carbon modification significantly boosts the maximum mass loading on the Ni foam, which is expected to endow the corresponding electrodes with favorably higher areal energy density.

The chemical composition of the NCM nanoneedles was characterized by XRD, FTIR, Raman, and XPS. Figure 3a shows that only the NCM2.0 and NCM3.0 samples show some distinct diffraction peaks in addition to the strong peaks at 44.3 and 51.7° belonging to the Ni foam substrate. This result is likely due to the higher mass loadings that render higher crystallinity and XRD peak intensity. The bare NCM2.0 was collected from NCM2.0@NC@Ni by strong sonication to exclude the implication of the Ni substrate. The XRD pattern in Figure 3b confirms the co-existence of $Ni_2(CO_3)(OH)_2$ (PDF no. 35-0501), $Co(CO_3)_{0.5}(OH)\cdot 0.11H_2O$ (PDF no. 48-0083), and $MnCO_3$ (PDF no. 86-0173) in NCM2.0.

Figure 3c exhibits the FTIR spectrum of NCM2.0. The broad peak at 3502 cm^{-1} corresponds to the stretching vibration of the O–H bond, indicative of the presence of the metal–OH layer. The peaks at 1449, 832, and 698 cm^{-1} are assigned to $\nu(OCO_2)$, $\nu(CO_3)$, and $\nu(OCO)$, respectively, confirming the existence of CO_3^{2-} in the sample.[51] Meanwhile, the peaks at 959 cm^{-1} refer to the bending vibration of Ni/Co–OH, while the one at 531 cm^{-1} corresponds to ρ_w (Co/Ni–OH).[25] The Raman spectrum (Figure 3d) shows two characteristic peaks at 1354 and 1578 cm^{-1}, ascribed to the D and G band of carbon, respectively. The D band is derived from the out-of-plane vibration of structural defects, while the G band origins from the in-plane vibration of sp^2 carbon.[52] Apart from that, the peaks at 548 and 630 cm^{-1} are ascribed to the vibration of Ni/Co–OH.[46] The peaks at 747 and 1089

https://doi.org/10.1021/acsami.1c12953
ACS Appl. Mater. Interfaces 2021, 13, 52519–52529

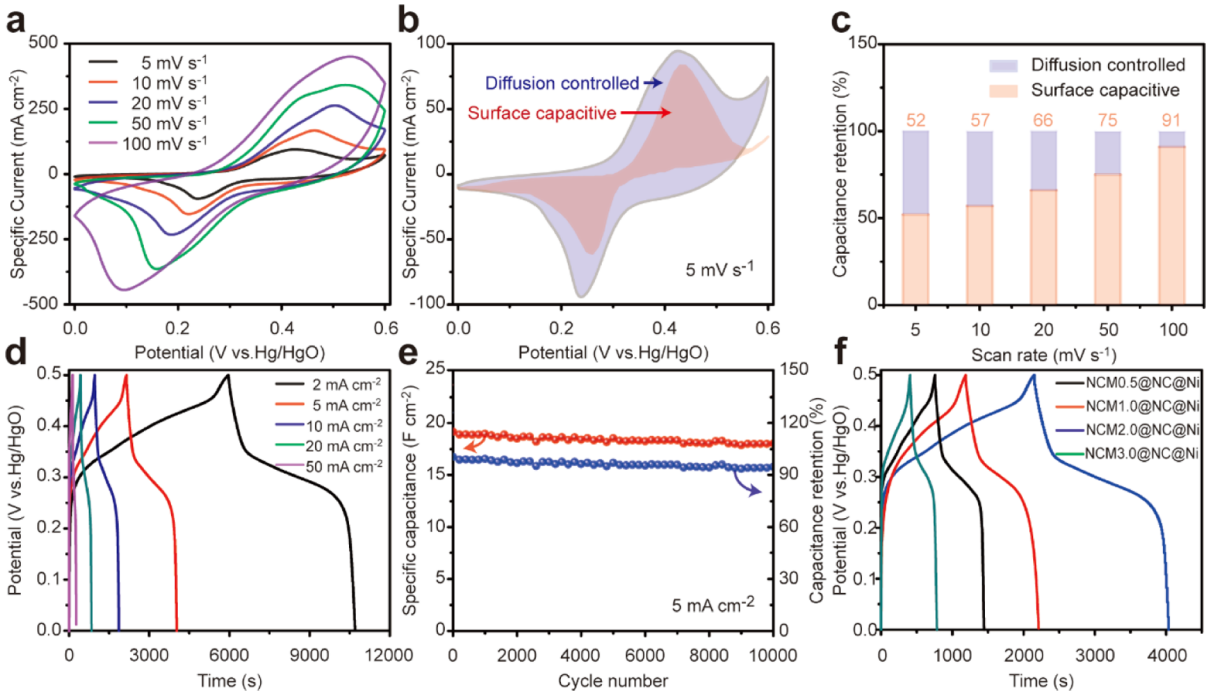

Figure 5. Electrochemical performance of NCM2.0@NC@Ni in three-electrode configuration: (a) CV curves at different scanning rates; (b,c) comparison of surface capacitive and diffusion-controlled contributions at different scanning rates; (d) GCD profiles at different current densities; and (e) long-term cycling performance at 5 mA cm^{-2}. (f) GCD profiles of different NCM@NC@Ni electrodes at 5 mA cm^{-2}.

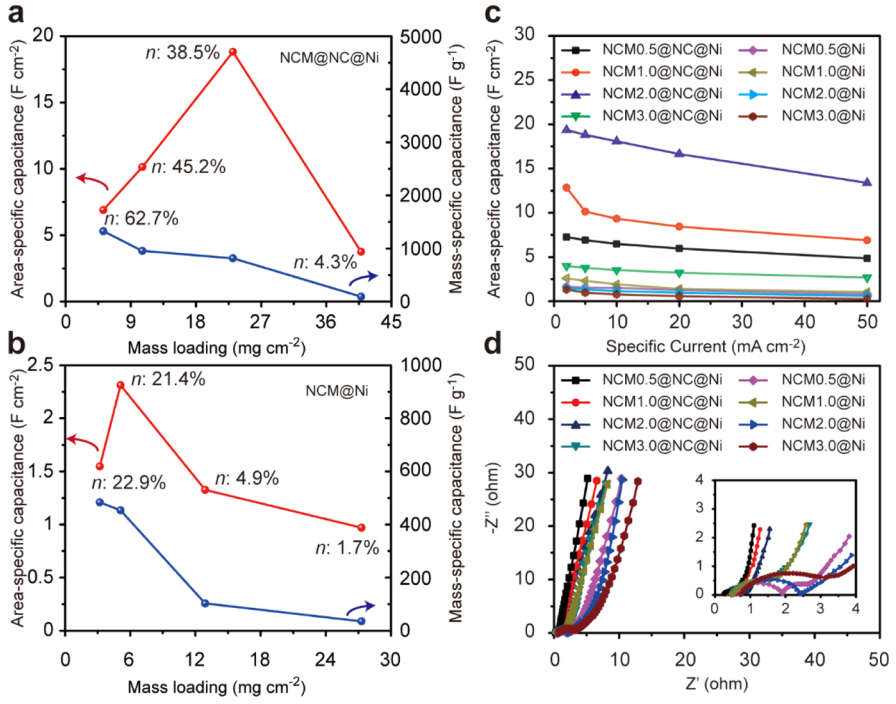

Figure 6. Relationship between the area/mass-specific capacitance (at 5 mA cm^{-2}), mass utilization (n), and mass loading of NCM on (a) NC@Ni and (b) pristine Ni foams; (c) rate performances and (d) Nyquist plots of all the NCM-based electrodes.

cm^{-1} are assigned to the stretching vibration modes of CO_3^{2-}, in good consistency with the reported literature.[53]

Moreover, XPS spectra were collected to elaborate further on the chemical state of NCM2.0 (Figure S4). The N 1s spectrum shows the typical character of the heteroatomic N doping in carbon lattice, while the C 1s and O 1s spectra confirm the existence of carbonate and hydroxyl in the obtained NCM. Meanwhile, all the metal species, including Ni^{2+}, Co^{2+}, and Mn^{2+}, can be detected in good accordance with the literature (see detailed analysis in the Supporting Information). All these results collectively determine the chemical composition of NCM as a ternary carbonate hydroxide of $Ni_2(CO_3)(OH)_2$, $Co(CO_3)_{0.5}(OH)\cdot 0.11H_2O$, and $MnCO_3$.

https://doi.org/10.1021/acsami.1c12953
ACS Appl. Mater. Interfaces 2021, 13, 52519−52529

Table 1. Comparison of the Mass Loading and Specific Capacitance with Representative Works

active materials	mass loading (mg cm^{-2})	specific capacitance	refs
$CoSe_2$/NC-NF	3.1	120.2 mA h g^{-1} at 1 A g^{-1}	28
NiCoMn carbonate hydroxide	3.7	3224 F g^{-1} at 1 A g^{-1}	56
$MnCo_2S_4$	4	231 mA h g^{-1} at 1 A g^{-1}	57
Mxene/BC	5	2.08 F cm^{-2} at 3 mA cm^{-2}	58
NiCoMn hydroxide	5.2	1043 μA h cm^{-2} at 2.5 mA cm^{-2}	26
$NiCo_2S_4$@Ni−Co LDH	5.6	5.68 F cm^{-2} at 2 mA cm^{-2}	59
MnO_2@CF	6.6	1.19 F cm^{-2} at 10 mA cm^{-2}	60
CDC@MnO_2	6.6	1.1 F cm^{-2} at 1 mA cm^{-2}	61
CNT/MnO_2/CC	9.1	3.38 F cm^{-2} at 1 mA cm^{-2}	62
$NiCo_2O_4$@NF	9.2	10.28 F cm^{-2} at 8 mA cm^{-2}	63
N-doped AC aerogel	10	386 F g^{-1} at 1 A g^{-1}	64
F-rGO	17	3.4 F cm^{-2} at 5 mA cm^{-2}	65
porous MnO_2 film	18	2.79 F cm^{-2} at 2 mA cm^{-2}	29
NCM2.0@NC@Ni	23.1	19.36 F cm^{-2} at 2 mA cm^{-2}	this work

Electron microscopy techniques (SEM, TEM, SAED, and EDX) were conducted to further probe into the microstructure of the NCM@NC@Ni. Representatively, the SEM images show that the NCM2.0@NC@Ni exhibits a distinctly different morphology compared with that of the NC@Ni substrate (Figure 4a). It is noticed that the NC@Ni frame is fully covered by massive and dense NCM nanoneedles (Figure 4b). The diameter of the nanoneedles is around 25 nm, as shown in magnified SEM and TEM images (Figure 4c,d). This array-like structure offers sufficient contact with the electrolyte and concurrently accommodates the volume expansion of NCM, thereby enhancing the reaction kinetic. The HRTEM image witnesses a lattice spacing of 0.238 nm (Figure 4e), corresponding to the (110) plane of $MnCO_3$. The lattice spacings of 0.245 and 0.227 nm in Figure 4e belong to the (301) and (231) planes of $Co(CO_3)_{0.5}(OH)\cdot 0.11H_2O$, respectively. Figure 4f shows the (240) and (141) planes of $Ni_2(CO_3)(OH)_2$ and the (113) plane of $MnCO_3$. The SAED rings in Figure 4g are well indexed to the (521), (141), and (220) planes of $Ni_2(CO_3)(OH)$. The EDX mapping and linear scanning analysis (Figure 4h−m) illustrate the uniform distribution of Ni, Co, and Mn elements in the nanoneedle. These results confirm the crystalline and compositional structure of the obtained NCM active material.

3.2. Electrochemical Performance. The electrochemical performance of the NCM2.0@NC@Ni electrode was first studied in a three-electrode system based on a 3.0 M KOH aqueous electrolyte. Figure 5a shows the CV curves at scan rates of 5, 10, 20, 50, and 100 mV s^{-1}. The reversible redox peaks at low rates suggest that the energy storage process is featured with the diffusion-controlled process. The redox reactions can be described as eqs 7−10. However, the redox peaks gradually weaken at high rates, while the curves transform into inclined rectangles, indicating that the surface capacitance increasingly dominates the energy storage.

$$Ni_2(CO_3)(OH)_2 + 4OH^- \leftrightarrow 2NiOOH + CO_3^{2-} + 2H_2O + 2e^- \quad (7)$$

$$Co(CO_3)_{0.5}(OH)\cdot 0.11H_2O + 2OH^- \leftrightarrow CoOOH + 0.5CO_3^{2-} + 1.11H_2O + e^- \quad (8)$$

$$MnCO_3 + 2OH^- \rightarrow Mn(OH)_2 + CO_3^{2-} \quad (9)$$

$$Mn(OH)_2 + OH^- \leftrightarrow MnOOH + H_2O + e^- \quad (10)$$

Figure 5b shows the capacitance distribution from the surface capacitive current (red) compared with the total capacitance (transparent) according to Dunn's method[54,55] (see details in the Supporting Information). The surface-controlled part accounts for 52% of the overall capacitance at 5 mV s^{-1}, continuously increasing to ∼91% at 100 mV s^{-1} (Figure 5c). Apart from that, the area-specific capacitances and Coulombic efficiencies calculated on GCD profiles are 19.36 F cm^{-2} (79.5%), 18.82 F cm^{-2} (87.3%), 18.08 F cm^{-2} (93.8%), 16.63 F cm^{-2} (97.0%), and 13.38 F cm^{-2} (98.4%) at the current density of 2, 5, 10, 20, and 50 mA cm^{-2}, respectively (Figure 5d). The low Coulombic efficiency at low current densities can be ascribed to a small reaction polarization. The lower overpotential leads to more severe oxygen evolution reactions and irreversible charge capacities at the same cutoff voltage. The mass-specific capacity at 2 mA cm^{-2} is 842 F g^{-1}, corresponding to a mass utilization (n) of 38.5%. Moreover, the long-term cycling measurement demonstrates high capacitance retention of 98% over 10,000 cycles (Figure 5e), indicating the great electrochemical reversibility and stabilities of NCM2.0@NC@Ni electrode attributed to the unique nanoneedle structure with high mass loading and strong structural integrity. In addition, the charge and discharge profiles of different NCMX@NC@Ni electrodes at 5 mA cm^{-2} are also presented in Figure 5f. The area-specific capacitance (utilization, mass loading) of the NCMX (X = 0.5, 1.0, 2.0, and 3.0) electrodes are 6.9 F cm^{-2} (62.7%, 5.2 mg cm^{-2}), 10.14 F cm^{-2} (45.2%, 10.6 mg cm^{-2}), 18.82 F cm^{-2} (38.5%, 23.1 mg cm^{-2}), and 3.76 F cm^{-2} (4.3%, 40.8 mg cm^{-2}), respectively. It is noticed that the NCM3.0@NC@Ni electrode delivers the highest mass loading and should hold the highest areal capacitance. However, such high mass loading deteriorates the uniformity of the nanoneedle-array structure and limits the utilization of active materials (n) and the mass-specific capacity. This result indicates that the electrodes are required to be rationally designed to balance this trade-off.

Figure 6a,b shows the relationship between the area/mass-specific capacitance, mass utilization (n), and mass loading of all the NCM@NC@Ni and NCM@Ni electrodes. In general, the two types of electrodes share a similar correlation between these parameters. One is that the mass-specific capacitance monotonously reduces with the increase of mass loading. A high mass loading results in material agglomeration and "dead volume," which deteriorates the kinetics, lessens the electrochemical sites, and decreases the mass utilization (n). The other is that the area-specific capacitance increases first and then reduces along with the rising loading. According to eq 2, the area-specific capacitance (C_a) is positively proportional to both mass utilization (n) and mass loading (m). The peak C_a

https://doi.org/10.1021/acsami.1c12953
ACS Appl. Mater. Interfaces 2021, 13, 52519−52529

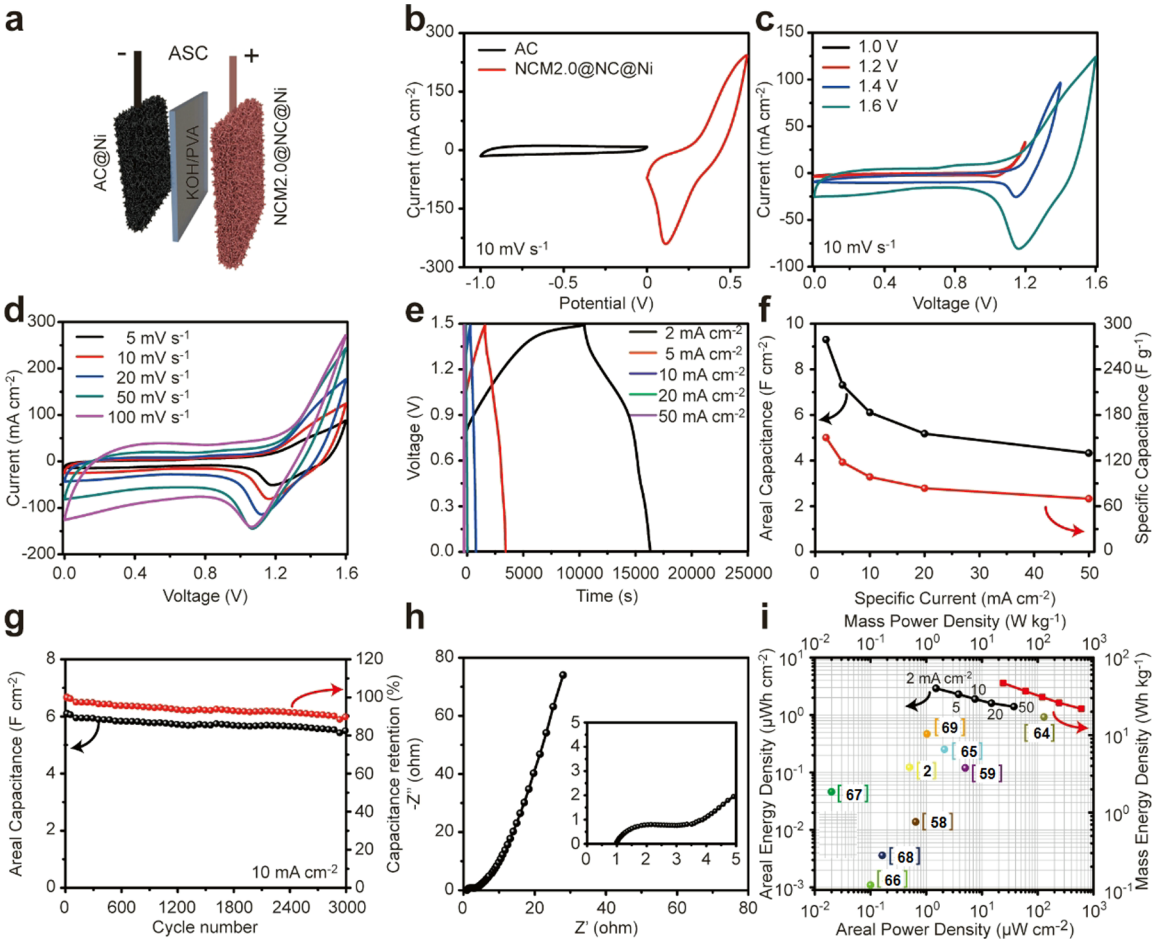

Figure 7. Electrochemical performances of solid-state asymmetric SC (ASC) in the configuration of NCM2.0@NC@Ni//AC: (a) schematic illustration of the ASC; (b) respective CV curves of NCM2.0@NC@Ni and AC electrodes at 10 mV s^{-1}; CV curves at different (c) voltage windows and (d) scan rates; (e) GCD profiles and (f) specific capacitance at different current densities; (g) cycling performance at 10 mA cm^{-2}; (h) EIS plot and (i) Ragone plots.

values are the trade-off result between these two factors. However, it is worth noting that the NCM*X*@NC@Ni (*X* = 0.5, 1.0, and 2.0) presents significantly higher capacitance, mass utilization, and mass loading than the NCM*X*@Ni counterparts, strongly confirming the tremendous structural and electrochemical advances by the as-developed surface carbon modification.

Figure 6c compares the rate performance of different NCM-based electrodes. Notably, all the NCM*X*@NC@Ni electrodes show much higher area-specific capacitance (C_a) than the NCM*X*@Ni electrodes at each current density. For example, at 5 mA cm^{-2}, the NCM2.0@NC@Ni shows a C_a of 18.82 F cm^{-2} with mass utilization of 38.5% and mass loading of 23.1 mg cm^{-2}, whereas these parameters are only 2.31 F cm^{-2}, 21.4%, and 5.1 mg cm^{-2}, respectively, for the NCM1.0@Ni counterpart. The carbon modification effectively boosts the maximum mass loading (m) and concurrently maintains a high mass utilization (n).

EIS characterization was used to illustrate the electrochemical impedance of the electrodes. All the NCM*X*@NC@Ni and NCM*X*@Ni electrodes show similar Nyquist plots (Figure 6d). The semicircle in the high-frequency region corresponds to the charge transfer resistance (R_{ct}), while the oblique line in the low-frequency region reflects the ion diffusion process (Wurberg resistance, W). It can be noticed that the R_{ct} and W values increase along with the NCM mass loading on a NC@Ni or Ni foam, suggesting the negative effect of mass loading on reaction kinetics. Nevertheless, the NCM*X*@NC@Ni electrode design consistently enables minor R_{ct} and W than NCM*X*@Ni electrodes at comparable mass loadings. This result indicates that surface modification by N-rich carbon nanosheets effectively preserves the nanoneedle architecture and remarkably improves overall electronic/ionic transport for fast reaction kinetics.

Table 1 compares the mass loading and area-specific capacity among NCM2.0@NC@Ni and other high-loading capacitive electrode designs in the recent literature. Our design enables significantly higher mass loading capability with higher achievable capacitance, mainly due to the highly favorable carbon modification. (I) The boosted SSA increases the contact area with both current collector and metal ions, allowing higher NCM growth on the substrate. (II) The well-maintained uniform nanoneedles under high mass loading provide significantly more active interfaces and enables excellent mass utilization than agglomerated or bulky structures for both capacitive and diffusion-controlled processes (eqs 7−10) thereon. Note that the reported NiCoMn carbonate hydroxide works generally emphasize the essential role of delicate nanostructure and composition in high-energy-density SCs.[56] However, this work focused on the

https://doi.org/10.1021/acsami.1c12953
ACS Appl. Mater. Interfaces 2021, 13, 52519−52529

modification of Ni foams and their influence on active materials' loading capability, microstructure, and electrochemical performance, using NCM as a model study.

According to eq 1, the area-specific energy density (E) is proportional to the voltage window (U) square that can be expanded using the ASC configuration. As shown in Figure 7a, the ASC was assembled using the NCM2.0@NC@Ni as the cathode, commercialized AC as the anode, and the PVA/KOH solid film as the electrolyte and separator. The CV curves confirm the reversible operation of NCM2.0@NC@Ni and AC electrodes at 0−0.6 and −1.0−0 V, respectively (Figure 7b). The performance of the AC electrode was examined by CV and GCD tests as shown in Figure S5, which confirms its typical EDLC character with a mass-specific capacity of ∼200 F g^{-1} at 0.5 A g^{-1}. Additionally, Figure 7c shows the CV profiles of the obtained ASC at varied voltage limits, revealing an accessible maximum voltage window up to 1.6 V. The CV curves (Figure 7d) and discharge profiles (Figure 7e) demonstrate a combination of Faradic and EDLC capacitive behaviors. Based on the discharge curve, the area-specific capacitances at 2, 5, 10, 20, and 50 mA cm^{-2} are 9.31, 7.31, 6.11, 5.18, and 4.33 F cm^{-2}, respectively (Figure 7f). Moreover, high capacitance retention of 78% can be achieved after 3000 cycles at 10 mA cm^{-2} (Figure 7g). The EIS plot reveals a favorably low internal impedance, contributing to the ASC's great electrochemical reversibility and rate capability. Beyond that, energy and power densities are two critical factors to evaluate the performance of energy storage devices. The area-specific energy density and power density of the as-developed ASC are 1352 μW h cm^{-2} (21.8 W h kg^{-1}) and 37,497 μW cm^{-2} (604.9 W kg^{-1}), respectively, significantly outperforming most of the reported ASCs[58,66−68] and symmetric SCs[2,59,64,65,69] (Figure 7i).

4. CONCLUSIONS

In summary, this work introduced N-doped carbon nanosheets to modify the Ni foams through a sol−gel method. The carbon nanosheets significantly boosted the SSA of Ni foams for maximizing the mass loading of NCM nanoneedles and concurrently maintains the well-defined nanoneedle structure for higher mass utilization and faster reaction kinetics. The trade-off among mass loading, mass utilization, and specific capacitance was systematically studied, while the optimized loading was obtained and employed for ASC evaluation. The NCM@NC@Ni electrode exhibits high mass loading up to 23.1 mg cm^{-2}, high capacitance of 19.36 F cm^{-2}, and excellent cyclability over 10,000 cycles. Moreover, the as-constructed NCM2.0@NC@Ni//AC asymmetric SC yields a high energy density of 1352 μW h cm^{-2}. This work presents a novel, facile, and effective surface modification strategy toward high-loading and high-energy-density solid-state SCs, providing instructive insights for developing advanced current collectors in related fields.

ASSOCIATED CONTENT

Supporting Information

The Supporting Information is available free of charge at https://pubs.acs.org/doi/10.1021/acsami.1c12953.

Calculation methods, additional experimental conditions, N_2 adsorption−desorption isotherms, SEM images, XPS spectra of NCM-based samples, and performance of the AC single electrode (PDF)

AUTHOR INFORMATION

Corresponding Authors

Liwei Su − *College of Chemical Engineering, Zhejiang University of Technology, Hangzhou 310014, China;* orcid.org/0000-0002-9791-3476; Phone: +86 571 88320611; Email: suliwei@zjut.edu.cn; Fax: +86 571 88320832

Lianbang Wang − *College of Chemical Engineering, Zhejiang University of Technology, Hangzhou 310014, China;* Email: wanglb99@zjut.edu.cn

Authors

Jing Zhan − *College of Chemical Engineering, Zhejiang University of Technology, Hangzhou 310014, China*

Gaoran Li − *College of Materials Science and Engineering, Nanjing University of Science and Technology, Nanjing 210094, China;* orcid.org/0000-0002-9336-6137

Qihang Gu − *College of Chemical Engineering, Zhejiang University of Technology, Hangzhou 310014, China*

Hao Wu − *College of Chemical Engineering, Zhejiang University of Technology, Hangzhou 310014, China*

Complete contact information is available at: https://pubs.acs.org/10.1021/acsami.1c12953

Author Contributions

[§]J.Z. and G.L. contributed equally to this work.

Notes

The authors declare no competing financial interest.

ACKNOWLEDGMENTS

This work was supported by the Natural Science Foundation of Zhejiang Province (LGG18B030001, LGG20B030002) and the National Natural Science Foundation of China (22075251, 22179118).

REFERENCES

(1) Halder, A.; Ghosh, M.; Khayum M, A.; Bera, S.; Addicoat, M.; Sasmal, H. S.; Karak, S.; Kurungot, S.; Banerjee, R. Interlayer Hydrogen-Bonded Covalent Organic Frameworks as High-Performance Supercapacitors. *J. Am. Chem. Soc.* **2018**, *140*, 10941−10945.

(2) Le, T. S.; Truong, T. K.; Huynh, V. N.; Bae, J.; Suh, D. Synergetic Design of Enlarged Surface Area and Pseudo-Capacitance for Fiber-Shaped Supercapacitor Yarn. *Nano Energy* **2020**, *67*, 104198.

(3) VahidMohammadi, A.; Mojtabavi, M.; Caffrey, N. M.; Wanunu, M.; Beidaghi, M. Assembling 2D MXenes into Highly Stable Pseudocapacitive Electrodes with High Power and Energy Densities. *Adv. Mater.* **2019**, *31*, 1970057.

(4) Pan, Z.; Yang, J.; Li, L.; Gao, X.; Kang, L.; Zhang, Y.; Zhang, Q.; Kou, Z.; Zhang, T.; Wei, L.; Yao, Y.; Wang, J. All-in-One Stretchable Coaxial-Fiber Strain Sensor Integrated with High-Performing Supercapacitor. *Energy Storage Mater.* **2020**, *25*, 124−130.

(5) Zhou, C.-A.; Yao, Z. J.; Xia, X. H.; Wang, X. L.; Gu, C. D.; Tu, J. P. Low-Strain Titanium-Based Oxide Electrodes for Electrochemical Energy Storage Devices: Design, Modification, and Application. *Mater. Today Nano* **2020**, *11*, 100085.

(6) Pan, Z.; Yang, J.; Zhang, Y.; Gao, X.; Wang, J. Quasi-Solid-State Fiber-Shaped Aqueous Energy Storage Devices: Recent Advances and Prospects. *J. Mater. Chem. A* **2020**, *8*, 6406−6433.

(7) Pan, Z.; Yang, J.; Zhang, Q.; Liu, M.; Hu, Y.; Kou, Z.; Liu, N.; Yang, X.; Ding, X.; Chen, H.; Li, J.; Zhang, K.; Qiu, Y.; Li, Q.; Wang, J.; Zhang, Y. All-Solid-State Fiber Supercapacitors with Ultrahigh Volumetric Energy Density and Outstanding Flexibility. *Adv. Energy Mater.* **2019**, *9*, 1802753.

(8) Jabeen, N.; Hussain, A.; Xia, Q.; Sun, S.; Zhu, J.; Xia, H. High-Performance 2.6 V Aqueous Asymmetric Supercapacitors Based on In

Situ Formed $Na_{0.5}MnO_2$ Nanosheet Assembled Nanowall Arrays. *Adv. Mater.* **2017**, *29*, 1700804.
(9) Wang, G.; Oswald, S.; Loffler, M.; Mullen, K.; Feng, X. Beyond Activated Carbon: Graphite-Cathode-Derived Li-Ion Pseudocapacitors with High Energy and High Power Densities. *Adv. Mater.* **2019**, *31*, 1807712.
(10) Sivakumar, P.; Jana, M.; Jung, M. G.; Gedanken, A.; Park, H. S. Hexagonal Plate-like Ni-Co-Mn Hydroxide Nanostructures to Achieve High Energy Density of Hybrid Supercapacitors. *J. Mater. Chem. A* **2019**, *7*, 11362−11369.
(11) Potphode, D.; Sayed, M. S.; Lama-Tamang, T.; Shim, J.-J. High-Performance Binder-Free Flower-like $(Ni_{0.66}Co_{0.3}Mn_{0.04})_2(OH)_2(CO_3)$ Array Synthesized Using Ascorbic Acid for Supercapacitor Applications. *Chem. Eng. J.* **2019**, *378*, 122129.
(12) Sun, S.; Zhai, T.; Liang, C.; Savilov, S. V.; Xia, H. Boosted Crystalline/Amorphous Fe_2O_3-δ Core/Shell Heterostructure for Flexible Solid-State Pseudocapacitors in Large Scale. *Nano Energy* **2018**, *45*, 390−397.
(13) Reghu Nath, A.; Jayachandran, A.; Sandhyarani, N. Nanosheets of Nickel, Cobalt and Manganese Triple Hydroxides/Oxyhydroxides as Efficient Electrode Materials for Asymmetrical Supercapacitors. *Dalton Trans.* **2019**, *48*, 4211−4217.
(14) Du, Y.; Li, G.; Chen, M.; Yang, X.; Ye, L.; Liu, X.; Zhao, L. Hollow Nickel-Cobalt-Manganese Hydroxide Polyhedra via MOF Templates for High-Performance Quasi-Solid-State Supercapacitor. *Chem. Eng. J.* **2019**, *378*, 122210.
(15) Liu, P.; Weng, X.; Liu, Z.; Zhang, Y.; Qiu, Q.; Wang, W.; Zhou, M.; Cai, W.; Ni, M.; Liu, M.; Liu, J. A High-Performance Quasi-Solid-State Supercapacitor Based on CuO Nanoparticles with Commercial-Level Mass Loading on Ceramic Material $La_{1-x}Sr_xCoO_3$-δ as Cathode. *ACS Appl. Energy Mater.* **2019**, *2*, 1480−1488.
(16) Jiang, H.; Ye, X.; Zhu, Y.; Yue, Z.; Wang, L.; Xie, J.; Wan, Z.; Jia, C. Flexible Solid-State Supercapacitors with High Areal Performance Enabled by Chlorine-Doped Graphene Films with Commercial-Level Mass Loading. *ACS Sustainable Chem. Eng.* **2019**, *7*, 18844−18853.
(17) Cai, X.; Song, Y.; Wang, S.-Q.; Sun, X.; Liu, X.-X. Extending the Cycle Life of High Mass Loading MoO_x Electrode for Supercapacitor Applications. *Electrochim. Acta* **2019**, *325*, 134877.
(18) Pan, Z.; Zhi, H.; Qiu, Y.; Yang, J.; Xing, L.; Zhang, Q.; Ding, X.; Wang, X.; Xu, G.; Yuan, H.; Chen, M.; Li, W.; Yao, Y.; Motta, N.; Liu, M.; Zhang, Y. Achieving Commercial-Level Mass Loading in Ternary-Doped Holey Graphene Hydrogel Electrodes for Ultrahigh Energy Density Supercapacitors. *Nano Energy* **2018**, *46*, 266−276.
(19) Egorov, V.; O'Dwyer, C. Architected Porous Metals in Electrochemical Energy Storage. *Curr. Opin. Electrochem.* **2020**, *21*, 201−208.
(20) Xu, J.; Zheng, F.; Xi, C.; Yu, Y.; Chen, L.; Yang, W.; Hu, P.; Zhen, Q.; Bashir, S. Facile Preparation of Hierarchical Vanadium Pentoxide (V_2O_5)/Titanium Dioxide (TiO_2) Heterojunction Composite Nano-Arrays for High Performance Supercapacitor. *J. Power Sources* **2018**, *404*, 47−55.
(21) Ouyang, B.; Zhang, Y.; Zhang, Z.; Fan, H. J.; Rawat, R. S. Nitrogen-Plasma-Activated Hierarchical Nickel Nitride Nanocorals for Energy Applications. *Small* **2017**, *13*, 1604265.
(22) Sanchez, J. S.; Pendashteh, A.; Palma, J.; Anderson, M.; Marcilla, R. Insights into Charge Storage and Electroactivation of Mixed Metal Sulfides in Alkaline Media: NiCoMn Ternary Metal Sulfide Nano-Needles Forming Core-Shell Structures for Hybrid Energy Storage. *J. Mater. Chem. A* **2019**, *7*, 20414−20424.
(23) Wu, Y.; Chen, H.; Lu, Y.; Yang, J.; Zhu, X.; Zheng, Y.; Lou, G.; Wu, Y.; Wu, Q.; Shen, Z.; Pan, Z. Rational Design of Cobalt-Nickel Double Hydroxides for Flexible Asymmetric Supercapacitor with Improved Electrochemical Performance. *J. Colloid Interface Sci.* **2021**, *581*, 455−464.
(24) Liang, M.; Zhao, M.; Wang, H.; Shen, J.; Song, X. Enhanced Cycling Stability of Hierarchical $NiCo_2S_4$@$Ni(OH)_2$@PPy Core−Shell Nanotube Arrays for Aqueous Asymmetric Supercapacitors. *J. Mater. Chem. A* **2018**, *6*, 2482−2493.
(25) Zhang, G.; Qin, P.; Nasser, R.; Li, S.; Chen, P.; Song, J. Synthesis of $Co(CO_3)_{0.5}(OH)$/$Ni_2(CO_3)(OH)_2$ Nanobelts and Their Application in Flexible All-Solid-State Asymmetric Supercapacitor. *Chem. Eng. J.* **2020**, *387*, 124029.
(26) Yang, S.; Wu, C.; Cai, J.; Zhu, Y.; Zhang, H.; Lu, Y.; Zhang, K. Seed-Assisted Smart Construction of High Mass Loading Ni-Co-Mn Hydroxide Nanoflakes for Supercapacitor Applications. *J. Mater. Chem. A* **2017**, *5*, 16776−16785.
(27) Bandyopadhyay, P.; Saeed, G.; Kim, N. H.; Lee, J. H. Zinc-Nickel-Cobalt Oxide@$NiMoO_4$ Core-Shell Nanowire/Nanosheet Arrays for Solid State Asymmetric supercapacitors. *Chem. Eng. J.* **2020**, *384*, 123357.
(28) Miao, C.; Xiao, X.; Gong, Y.; Zhu, K.; Cheng, K.; Ye, K.; Yan, J.; Cao, D.; Wang, G.; Xu, P. Facile Synthesis of Metal-Organic Framework-Derived $CoSe_2$ Nanoparticles Embedded in the N-Doped Carbon Nanosheet Array and Application for Supercapacitors. *ACS Appl. Mater. Interfaces* **2020**, *12*, 9365−9375.
(29) Yang, J.; Lian, L.; Ruan, H.; Xie, F.; Wei, M. Nanostructured Porous MnO_2 on Ni Foam Substrate with a High Mass Loading via a CV Electrodeposition Route for Supercapacitor Application. *Electrochim. Acta* **2014**, *136*, 189−194.
(30) Zhang, G.; Hu, J.; Nie, Y.; Zhao, Y.; Wang, L.; Li, Y.; Liu, H.; Tang, L.; Zhang, X.; Li, D.; Sun, L.; Duan, H. Integrating Flexible Ultralight 3D Ni Micromesh Current Collector with NiCo Bimetallic Hydroxide for Smart Hybrid Supercapacitors. *Adv. Funct. Mater.* **2021**, *31*, 2100290.
(31) Zhao, H.-B.; Zhou, X.-C.; Fu, Z.-B.; Mi, R.; Wang, C.-Y. Freestanding Monolithic Ni Aerogel with Large Surface Areas from Cellulose Aerogel Templates. *Mater. Lett.* **2017**, *196*, 296−299.
(32) Woo, S.; Nam, D.; Chang, W.; Ko, Y.; Lee, S.; Song, Y.; Yeom, B.; Moon, J. H.; Lee, S. W.; Cho, J. A Layer-by-Layer Assembly Route to Electroplated Fibril-Based 3D Porous Current Collectors for Energy Storage Devices. *Small* **2021**, *17*, 2007579.
(33) Wang, Z.; Yan, Y.; Chen, Y.; Han, W.; Liu, M.; Zhang, Y.; Xiong, Y.; Chen, K.; Lv, Z.; Liu, M. 3D-Hierarchical Porous Nickel Sculptured by a Simple Redox Process and Its Application in High-Performance Supercapacitors. *J. Mater. Chem. A* **2017**, *5*, 20709−20719.
(34) Grden, M.; Alsabet, M.; Jerkiewicz, G. Surface Science and Electrochemical Analysis of Nickel Foams. *ACS Appl. Mater. Interfaces* **2012**, *4*, 3012−3021.
(35) Lyu, L.; Kang, J.; Seong, K.-d.; Kim, C. W.; Lim, J.; Piao, Y. ZnNiCo Hydroxide/Graphene-Carbon Nanotube Hydrogel on Surface-Modified Ni Foam as a Battery-Type Electrode for Hybrid Supercapacitors. *J. Alloys Compd.* **2021**, *872*, 159610.
(36) Hu, C.; Miao, L.; Yang, Q.; Yu, X.; Song, L.; Zheng, Y.; Wang, C.; Li, L.; Zhu, L.; Cao, X.; Niu, H. Self-Assembly of CNTs on Ni Foam for Enhanced Performance of $NiCoO_2$@CNT@NF Supercapacitor Electrode. *Chem. Eng. J.* **2021**, *410*, 128317.
(37) Meng, W.; Du, X.; Lin, Z.; Li, W. Facile Flame Deposition of Carbon Coating onto Ni Foam and the Study of the Derived Carbon Foam with High Capacitive Performance. *Surf. Coat. Technol.* **2020**, *401*, 126246.
(38) Mariappan, V. K.; Krishnamoorthy, K.; Pazhamalai, P.; Sahoo, S.; Kim, S.-J. Carbyne-Enriched Carbon Anchored on Nickel Foam: A Novel Binder-Free Electrode for Supercapacitor Application. *J. Colloid Interface Sci.* **2019**, *556*, 411−419.
(39) Zhao, J.; Zou, X.; Sun, P.; Cui, G. Three-Dimensional Bi-Continuous Nanoporous Gold/Nickel Foam Supported MnO_2 for High Performance Supercapacitors. *Sci. Rep.* **2017**, *7*, 17857.
(40) Peng, Z.; Guo, Y.; Chen, C.; Ao, G.; Wang, X.; Wang, S.; Zhang, Y.; Lv, Z.; Wang, Z. Porous and Wrinkle Treatment of Commercial Ni Foam and Its Application for High-Efficiency Oxygen Evolution Reaction Electrode. *Int. J. Hydrogen Energy* **2021**, *46*, 4890−4902.
(41) Qin, H.; Zhen, C.; Jia, C.; Yang, Z.; Ye, H.; Cheng, H.-M.; Liu, G. An Oxidation-Nitridation-Denitridation Approach to Transform

Metal Solids into Foams with Adjustable Pore Sizes for Energy Applications. *Sci. Bull.* **2021**, *66*, 1525−1532.
(42) Wu, B.; Zhang, F.; Nie, Z.; Qian, H.; Liu, P.; He, H.; Wu, J.; Chen, Z.; Chen, S. A High-Performance Battery-like Supercapacitor Electrode with a Continuous NiTe Network Skeleton Running throughout $Co(OH)_2/Co_9S_8$ Nanohybrid. *Electrochim. Acta* **2021**, *365*, 137325.
(43) Zhao, Y.; Ma, H.; Huang, S.; Zhang, X.; Xia, M.; Tang, Y.; Ma, Z.-F. Monolayer Nickel Cobalt Hydroxyl Carbonate for High Performance All-Solid-State Asymmetric Supercapacitors. *ACS Appl. Mater. Interfaces* **2016**, *8*, 22997−23005.
(44) Xia, Q. X.; San Hui, K.; Hui, K. N.; Kim, S. D.; Lim, J. H.; Choi, S. Y.; Zhang, L. J.; Mane, R. S.; Yun, J. M.; Kim, K. H. Facile Synthesis of Manganese Carbonate Quantum Dots/$Ni(HCO_3)_2$−$MnCO_3$ Composites as Advanced Cathode Materials for High Energy Density Asymmetric Supercapacitors. *J. Mater. Chem. A* **2015**, *3*, 22102−22117.
(45) Yu, Z.; Chen, Y.; Cheng, Z.; Tsekouras, G.; Li, X.; Wang, X.; Kong, X.; Dou, S. X. Enzyme-Catalysed Room Temperature and Atmospheric Pressure Synthesis of Metal Carbonate Hydroxides for Energy Storage. *Nano Energy* **2018**, *54*, 200−208.
(46) Ji, X.; Cheng, S.; Yang, L.; Jiang, Y.; Jiang, Z.-j.; Yang, C.; Zhang, H.; Liu, M. Phase Transition−Induced Electrochemical Performance Enhancement of Hierarchical $CoCO_3$/CoO Nanostructure for Pseudocapacitor Electrode. *Nano Energy* **2015**, *11*, 736−745.
(47) Qu, Y.; Zan, G.; Wang, J.; Wu, Q. Preparation of Eggplant-Derived Macroporous Carbon Tubes and Composites of EDMCT/$Co(OH)(CO_3)_{0.5}$ Nano-Cone-Arrays for High-Performance Supercapacitors. *J. Mater. Chem. A* **2016**, *4*, 4296−4304.
(48) Su, L.; Zhou, Z.; Shen, P. Ni/C Hierarchical Nanostructures with Ni Nanoparticles Highly Dispersed in N-Containing Carbon Nanosheets: Origin of Li Storage Capacity. *J. Phys. Chem. C* **2012**, *116*, 23974−23980.
(49) Zhang, M.; Liu, H.; Song, Z.; Ma, T.; Xie, J. Self-Assembling $NiCo_2S_4$ Nanorods Arrays and T-Nb_2O_5 Nanosheets/Three-Dimensional Nitrogen-Doped Garphene Hybrid Nanoarchitectures for Advanced Asymmetric Supercapacitor. *Chem. Eng. J.* **2020**, *392*, 123669.
(50) Zheng, L.; Guan, L.; Song, J.; Zheng, H. Rational Design of a Sandwiched Structure $Ni(OH)_2$ Nanohybrid Sustained by Amino-Functionalized Graphene Quantum Dots for Outstanding Capacitance. *Appl. Surf. Sci.* **2019**, *480*, 727−737.
(51) Leng, X.; Wu, L.; Liu, Y.; Li, C.; Wei, S.; Jiang, Z.; Wang, G.; Lian, J.; Jiang, Q. A Novel Open Architecture Built by Ultra-Fine Single-Crystal $Co_2(CO_3)(OH)_2$ Nanowires and Reduced Graphene Oxide for Asymmetric Supercapacitors. *J. Mater. Chem. A* **2016**, *4*, 17171−17179.
(52) Zhang, J.; Zhao, H.; Li, J.; Jin, H.; Yu, X.; Lei, Y.; Wang, S. In Situ Encapsulation of Iron Complex Nanoparticles into Biomass-Derived Heteroatom-Enriched Carbon Nanotubes for High-Performance Supercapacitors. *Adv. Energy Mater.* **2019**, *9*, 1803221.
(53) Yuan, P. W.; Guo, S. H.; Gao, S. Q.; Wang, J.; Chen, W. Q.; Li, M.; Ma, K. Y.; Wang, N.; Liu, F.; Cheng, J. P. Influence of Ni/Cu Ratio in Nickel Copper Carbonate Hydroxide on the Phase and Electrochemical Properties. *J. Alloys Compd.* **2019**, *780*, 147−155.
(54) Augustyn, V.; Come, J.; Lowe, M. A.; Kim, J. W.; Taberna, P.-L.; Tolbert, S. H.; Abruña, H. D.; Simon, P.; Dunn, B. High-Rate Electrochemical Energy Storage through Li^+ Intercalation Pseudocapacitance. *Nat. Mater.* **2013**, *12*, 518−522.
(55) Chao, D.; Zhu, C.; Yang, P.; Xia, X.; Liu, J.; Wang, J.; Fan, X.; Savilov, S. V.; Lin, J.; Fan, H. J.; Shen, Z. X. Array of Nanosheets Render Ultrafast and High-Capacity Na-Ion Dtorage by Tunable Pseudocapacitance. *Nat. Commun.* **2016**, *7*, 12122.
(56) Zhong, Y.; Cao, X.; Liu, Y.; Cui, L.; Liu, J. Nickel Cobalt Manganese Ternary Carbonate Hydroxide Nanoflakes Branched on Cobalt Carbonate Hydroxide Nanowire Arrays as Novel Electrode Material for Supercapacitors with Outstanding Performance. *J. Colloid Interface Sci.* **2021**, *581*, 11−20.
(57) Abbasi, L.; Arvand, M.; Moosavifard, S. E. Facile Template-Free Synthesis of 3D Hierarchical Ravine-like Interconnected $MnCo_2S_4$ Nanosheet Arrays for Hybrid Energy Storage Device. *Carbon* **2020**, *161*, 299−308.
(58) Wang, Y.; Wang, X.; Li, X.; Bai, Y.; Xiao, H.; Liu, Y.; Liu, R.; Yuan, G. Engineering 3D Ion Transport Channels for Flexible MXene Films with Superior Capacitive Performance. *Adv. Funct. Mater.* **2019**, *29*, 1900326.
(59) Wang, Y.-F.; Wang, H.-T.; Yang, S.-Y.; Yue, Y.; Bian, S.-W. Hierarchical $NiCo_2S_4$@Nickel-Cobalt Layered Double Hydroxide Nanotube Arrays on Metallic Cotton Yarns for Flexible Supercapacitors. *ACS Appl. Mater. Interfaces* **2019**, *11*, 30384−30390.
(60) Chodankar, N. R.; Patil, S. J.; Rama Raju, G. S.; Lee, D. W.; Dubal, D. P.; Huh, Y. S.; Han, Y. K. Two-Dimensional Materials for High-Energy Solid-State Asymmetric Pseudocapacitors with High Mass Loadings. *ChemSusChem* **2020**, *13*, 1582−1592.
(61) Zhang, Y.; Yuan, X.; Lu, W.; Yan, Y.; Zhu, J.; Chou, T.-W. MnO_2 Based Sandwich Structure Electrode for Supercapacitor with Large Voltage Window and High Mass Loading. *Chem. Eng. J.* **2019**, *368*, 525−532.
(62) Lyu, L.; Seong, K.-d.; Kim, J. M.; Zhang, W.; Jin, X.; Kim, D. K.; Jeon, Y.; Kang, J.; Piao, Y. CNT/High Mass Loading MnO_2/Graphene-Grafted Carbon Cloth Electrodes for High-Energy Asymmetric Supercapacitors. *Nano-Micro Lett.* **2019**, *11*, 88.
(63) Tong, Z.; Ji, Y.; Tian, Q.; Ouyang, W. High Mass Loading and High-Density Flower-like $NiCo_2O_4$ Nanosheets on Ni Foam for Superior Capacitance. *Chem. Commun.* **2019**, *55*, 9128−9131.
(64) Wang, D.; Fan, W.; Yuan, S.; Liu, T. Improving Hierarchical Porous Structure of Carbon Aerogels for More Efficient Ion Transport for Supercapacitors with Commercial Level Mass Loading. *Electrochim. Acta* **2019**, *323*, 134811.
(65) Zhu, Y.; Jiang, H.; Ye, X.; Yue, Z.; Wang, L.; Jia, C. Similar "Relay Race" Capacitance Behaviors of Folded Graphene Films Based High-Performance Supercapacitors. *J. Power Sources* **2020**, *460*, 228108.
(66) Zhang, X.; Fu, Q.; Huang, H.; Wei, L.; Guo, X. Silver-Quantum-Dot-Modified MoO_3 and MnO_2 Paper-like Freestanding Films for Flexible Solid-State Asymmetric Supercapacitors. *Small* **2019**, *15*, 1805235.
(67) Su, F.; Lv, X.; Miao, M. High-Performance Two-Ply Yarn Supercapacitors Based on Carbon Nanotube Yarns Dotted with Co_3O_4 and NiO Nanoparticles. *Small* **2015**, *11*, 854−861.
(68) Tang, T.; Cui, S.; Chen, W.; Hou, H.; Mi, L. Bio-Inspired Nano-Engineering of an Ultrahigh Loading 3D Hierarchical Ni@$NiCo_2S_4/Ni_3S_2$ Electrode for High Energy Density Supercapacitors. *Nanoscale* **2019**, *11*, 1728−1736.
(69) Wechsler, S. C.; Amir, F. Z. Superior Electrochemical Performance of Pristine Nickel Hexaaminobenzene MOF Supercapacitors Fabricated by Electrophoretic Deposition. *ChemSusChem* **2020**, *13*, 1491−1495.

https://doi.org/10.1021/acsami.1c12953
ACS Appl. Mater. Interfaces 2021, 13, 52519−52529